Ultrasound Scattering From Cell-Pellet Biophantoms and *Ex Vivo* Tumors Provides Insight Into the Cellular Structure Involved in Scattering

Pauline Muleki-Seya and William D. O'Brien, *Life Fellow, IEEE*

***Abstract*— The histologically identifiable cellular structure(s) involved in ultrasonic scattering is(are) yet to be uniquely identified. The study quantifies six possible cellular scattering parameters, namely, cell and nucleus radii and their respective cell and nucleus volume fractions as well as a combination of cell and nucleus radii and their volume fraction. The six cellular parameters are each derived from four cell lines (4T1, JC, LMTK, and MAT) and two tissue types (cell-pellet biophantom and *ex vivo* tumor). Optical histology and quantitative ultrasound (QUS), both independent approaches, are used to yield these cellular parameters. QUS scatterer parameters are experimentally determined using two ultrasonic scattering models: the spherical Gaussian model (GM) and the structure factor model (SFM) to yield insight about scattering from nuclei only and cells only. GM is a classical ultrasonic scattering model to evaluate QUS parameters and is well adapted for diluted media. SFM is adapted for dense media to estimate reasonably well scatterer parameters of cellular structures from *ex vivo* tissue. Nucleus and cell radii and volume fractions are measured optically from histology. They were used as inputs to calculate BSC for scattering from cells, nuclei, and both cells and nuclei. The QUS-derived scatterers (radii and volume fractions) distributions were then compared to the optical histology scatterer parameters derived from these calculated BSCs. The results suggest scattering from cells only (LMTK and MAT) or both cells and nuclei (4T1 and JC) for cell-pellet biophantoms and scattering from nuclei only for tumors.**

***Index Terms*— Backscatter coefficient (BSC), cell-pellet biophantoms, *ex vivo tissues*, scattering source.**

Manuscript received July 9, 2021; accepted November 22, 2021. Date of publication November 25, 2021; date of current version January 26, 2022. This work was supported in part by NIH under Grant R37EB002641 and Grant R01CA226528 and in part by the French National Research Agency (ANR) performed within the framework of the LABEX PRIMES (ANR-11-LABX-0063) of the Université de Lyon, through the Program "Investissements d'Avenir" (ANR-11-IDEX-0007). *(Corresponding author: Pauline Muleki-Seya.)*

This work involved animals in its research. Approval of all ethical and experimental procedures and protocols was granted by the Institutional Animal Care and Use Committee of the University of Illinois under Protocol No. 16010.

Pauline Muleki-Seya is with Univ Lyon, INSA-Lyon, Université Claude Bernard Lyon 1, UJM-Saint Etienne, CNRS, Inserm, CREATIS UMR 5220, U1294, 69100 Villeurbanne, France (e-mail: pauline.muleki-seya@creatis.insa-lyon.fr).

William D. O'Brien is with the Bioacoustics Research Laboratory, Department of Electrical and Computer Engineering, University of Illinois at Urbana–Champaign, Urbana, IL 61801 USA.

This article has supplementary downloadable material available at https://doi.org/10.1109/TUFFC.2021.3130682, provided by the authors.

Digital Object Identifier 10.1109/TUFFC.2021.3130682

I. Introduction

CELL-PELLET (CP) biophantoms are composed of densely packed cells and are often used to mimic tumors in quantitative ultrasound (QUS) studies. These CP-biophantom-based QUS studies have been used to address tissue characterizations [1]–[7] or monitor cell death applications [8], [9] by apoptosis [10] or mitotic arrest [11]. QUS provides information about tissue microstructure and is based on analyses of ultrasonic backscattered signals or more specifically the backscatter coefficient (BSC). Then, ultrasonic scatterer parameters (radius, acoustic concentration, volume fraction, and relative impedance contrast) are estimated by fitting a theoretical BSC derived from an ultrasonic scattering model to the experimentally derived BSC.

To determine whether CP biophantoms provide adequate tumor models, it is necessary to demonstrate that the histologically identifiable cellular structure(s) involved in ultrasonic scattering is(are) closely related between biophantoms and tumors. However, the ultrasonic scattering structure(s) at the cellular level is(are) still not identified. The challenge may result from inadequate ultrasonic scattering models. Classically employed scattering models [spherical Gaussian model (GM), fluid sphere model, and so on] are adapted for dilute media that satisfy the condition of random and independent distribution of scatterers. However, the dilute-media condition is not satisfied for dense-media CP biophantoms [3] or tumors that have densely packed cells [9]. The structure factor model (SFM) is better adapted for dense media [12] because, unlike the classical ultrasonic models that consider only incoherent scattering by summing the contributions from individual ultrasonic scatterers, the SFM considers also the scatterers' interactions using a statistical mechanics structure factor [13], [14]. A previous study [12] suggested that the main ultrasonic scattering structure from canine liver was the hepatocyte nucleus and from HT29 mouse tumors was the whole cell. Another study [15] suggested that the nucleus was the dominant scattering source in rabbit liver based on a 3-D impedance map study. By comparing cell-pellet biophantoms and corresponding isolated nuclei biophantoms with different nuclei sizes, Taggard *et al.* [16] concluded that the BSC was correlated with the size of nuclei. Other studies based mainly on the effect of apoptosis on ultrasonic

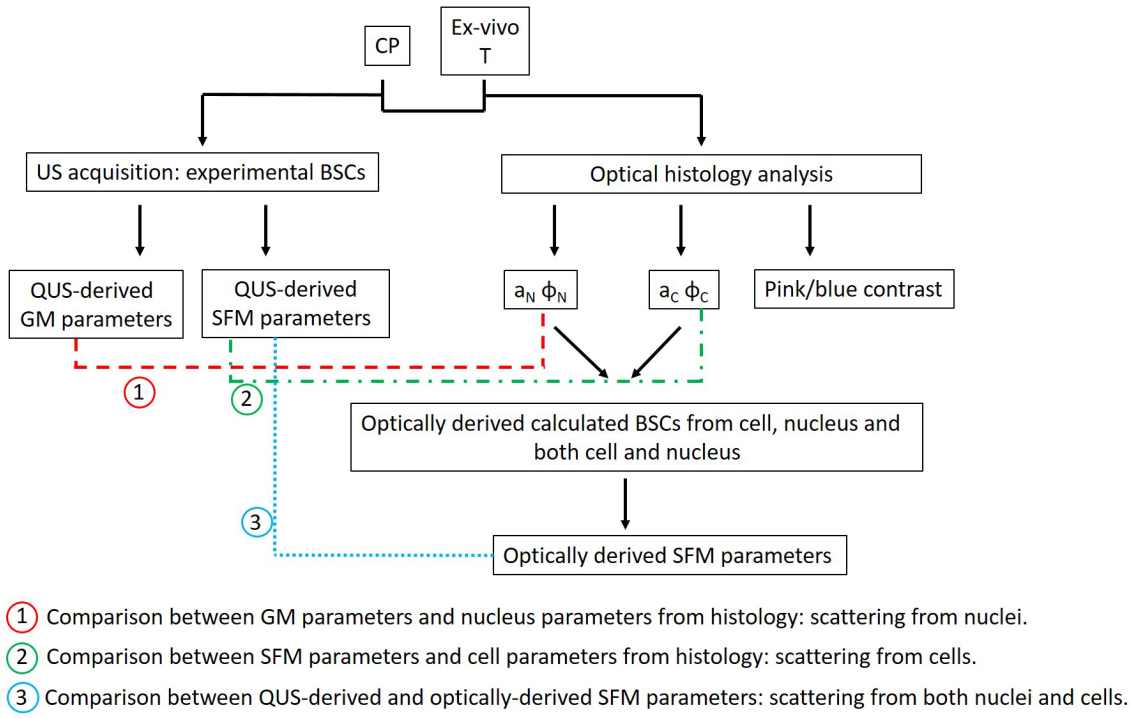

Fig. 1. Schematic of the study. a_N, ϕ_N, a_C, and ϕ_C denote the radii and volume fractions from nuclei and cells.

backscattering have suggested that the nucleus was the major scattering source [17]–[19].

There is significant scientific value to elucidate the ultrasonic scattering structure(s), particularly at the cellular scale. Fundamentally, this is of great relevance for developing novel imaging and diagnostic capabilities from the first principles. For example, if CP biophantoms are equivalent models of tumors for tissue characterization applications, then simpler nonanimal-based experimental approaches might become readily available, thus broadening the capability and productivity of laboratory-based studies.

The study's objective is to gain insight into the cellular structure(s) that is(are) involved in ultrasonic scattering. For that, the same four cell lines are utilized in both CP biophantoms and *ex vivo* tumors (T). There are three main study objectives (Fig. 1). First, determine whether nuclei only or cells only are involved in ultrasonic scattering from the CP biophantoms and *ex vivo* tumors. For that, the QUS-derived scatterer parameters from experimental BSC outcomes using spherical GM and SFM are compared to the nucleus and cell radii and volume fractions (respectively, tracks 1 and 2, Fig. 1); this approach is based on the following assumptions. If scattering from nuclei only is considered, then the BSC would consist of an incoherent contribution, and the GM should provide reasonably accurate parameter estimates of nuclei. If scattering from cells only is considered, then the BSC would consist of both incoherent and coherent contributions, and the SFM should provide reasonably accurate parameter estimates of cells. The approach in this part of the study is similar to our previous study [12]. Second, evaluate whether both cells and nuclei are involved in ultrasonic scattering from CP biophantoms and *ex vivo* tumors. For that, the optical histology-measured parameters (mean nucleus and cell radii and volume fractions) from CP biophantoms and *ex vivo* tumors are used as inputs to evaluate BSCs with a simple scattering model from cells, nuclei, and both cells and nuclei. Then, optical histology-derived scatterer parameters are estimated and compared to the QUS-derived outcomes (track 3, Fig. 1). This model and its methodology are the main contributions of this study. Third, determine whether the main ultrasonic scatterers are different between the four cell lines from CP biophantoms and *ex vivo* tumors. For that, the optically derived nucleus and cell radii and their volume fractions are compared among the different cell lines. Also, pink and blue contrasts from nuclei and cells optically derived from H&E staining are evaluated to provide relative information about their acoustic impedance.

II. Material and Methods

A. Glossary

The main terms used in the study and their definitions are summarized in Table I.

B. CP Biophantoms and Ex Vivo Tumors (T)

The CP biophantoms are composed of a large number of densely packed cells without any supportive background materials. Four tumor cell lines are used to create the CP biophantoms: 13762 MAT B III (MAT) mammary adenocarcinoma (ATCC CRL-1666), 4T1 mammary carcinoma (ATCC CRL-2539), JC mammary adenocarcinoma (ATCC CRL-2116), and LMTK soft-tissue sarcoma (ATCC CCL-1.3), denoted MAT, 4T1, JC, and LMTK, respectively. The experimental procedure to fabricate CP biophantoms has been described in [2]; 3 MAT, 16 4T1, 10 JC, and 15 LMTK independent CP replicates are ultrasonically scanned and analyzed.

TABLE I
MAIN TERMS USED IN THE STUDY AND THEIR DEFINITIONS

Term	Definition
Experimental BSC	BSC evaluated from experimental ultrasonic acquisition
QUS-derived parameters	Scatterer parameters evaluated from experimental BSC: scatterer radius and acoustic concentration using GM and scatterer radius, volume fraction and relative impedance contrast using SFM
Optical histology-measured parameters	Cells and nuclei radii and volume fractions measured on histological images
Calculated BSC	BSC evaluated with SFM model using the mean optical-histology parameters as income
Optical histology-derived parameters	Scatterer parameters evaluated from calculated BSC: scatterer radius, volume fraction and relative impedance contrast using SFM

TABLE II
MEAN ATTENUATION COEFFICIENTS AND STANDARD DEVIATIONS FOR EACH TISSUE TYPE (CP AND T). THE ATTENUATION COEFFICIENTS CORRESPOND TO αf^n WHERE f DENOTES THE FREQUENCY

	CP		T	
	α (dB/cm)	n	α (dB/cm)	n
4T1	0.13 ± 0.03	1.42 ± 0.05	0.14 ± 0.03	1.42 ± 0.05
JC	0.14 ± 0.06	1.43 ± 0.08	0.21 ± 0.05	1.32 ± 0.08
LMTK	0.18 ± 0.03	1.34 ± 0.04	0.13 ± 0.04	1.46 ± 0.07
MAT	0.06 ± 0.01	1.58 ± 0.02	0.18 ± 0.07	1.41 ± 0.07

Tumors are grown in mice and rats (Harlan Laboratories, Inc., Indianapolis, IN, USA) using the same CP cell lines: 13 Fischer 344 rats (MAT tumors), 20 BALB/c mice (13 mice with 4T1 tumors and 7 mice with JC tumors), and 8 Nude-Foxn1nu mice (LMTK tumors). The MAT, 4T1, JC, and LMTK cells are injected into rats or mice. The animals are anesthetized with isoflurane before subcutaneous and bilateral cell injection into the mammary fat pad. The injection volume is 100 μL (containing 500 cells for MAT and 4T1, 2×10^5 cells for JC, and 10^4 cells for LMTK) or 50 μL (containing 10^5 MAT cells). The tumor size was regularly monitored *in vivo* both manually and using a Vevo 2100 system (VisualSonics Inc., Toronto, ON, Canada). Tumors were allowed to grow to about 5 mm in diameter. The animals were then euthanized via CO_2 and the tumors were excised and placed on a planar Plexiglas plate; 18 MAT, 22 4T1, 10 JC, and 13 LMTK independent tumor replicates were excised, ultrasonically scanned, and analyzed.

The experimental protocol was approved by the Institutional Animal Care and Use Committee of the University of Illinois and satisfied all campus and National Institutes of Health rules for the humane use of laboratory animals. Animals were housed in an approved Association for Assessment and Accreditation of Laboratory Animal Care (Rockville, MD, USA) animal facility and provided food and water ad libitum.

C. QUS Acquisition From CP Biophantoms and Ex Vivo Tumors

A single-element, weakly focused 40-MHz transducer (High Frequency Transducer Resource Center, USC, Los Angeles, CA, USA, −10-dB bandwidth of 25–55 MHz) was used to scan CPs and Ts. The transducer was interfaced with a UTEX UT340 pulser/receiver (UTEX Scientific Instruments Inc., Mississauga, ON, Canada) that operated in the pitch-catch mode. A 50DR-001 BNC attenuator (JFW Industries Inc., Indianapolis, IN, USA) was connected to the pulser to attenuate the driving pulse to avoid transducer saturation. An RDX-6 diplexer (Ritec Inc., Warwick, RI, USA) was used to separate the transmitted and received signals because only the transmitted signal needed to be attenuated. The received radio frequency (RF) signals were acquired using a 10-bit Agilent U1065A-002 A/D (Agilent Technologies, Santa Clara, CA, USA) set to sample at 1 GHz. The ultrasonic transducer was moved using a precision motion control system (Daedal Parker Hannifin Corporation, Irwin, PA, USA) with a linear spatial accuracy of 1 μm. The samples were placed on the Plexiglas plate during ultrasonic scans. The scans were performed at room temperature in a small tank filled with DPBS (Dulbecco's phosphate-buffered saline) for CP or saline for T.

Ultrasonic attenuation and BSC measurements were both performed for all CP and T samples. Attenuation values were acquired using an insertion-loss broadband technique [20] and used to yield accurate BSC values because of the large attenuation values at the ultrasonic frequencies used herein. The insertion loss was determined by comparing the power spectra of the echoes reflected off the Plexiglas surface with and without the sample inserted in the ultrasonic propagation path. The effect of DPBS or saline attenuation was compensated for. The attenuation (dB/cm) of each sample was generated by averaging the attenuation obtained from 36 independent locations across the sample, and the mean attenuation coefficients are summarized in Table II. The BSC scanning procedure has been described in [2]. For each sample, 11 independent scans were recorded. A mean BSC was estimated for each of the 11 scans by averaging the BSCs from different regions of interest (ROIs) within that scan (ROIs correspond to 75%-overlapped regions with dimensions 0.56×0.56 mm^2, equivalent to 15×15 wavelengths at 40 MHz). Then, for each CP and T sample, 11 mean BSCs were used to estimate the ultrasonic scatterer parameters.

D. Optical Evaluations From Histology Images

Immediately after ultrasonic scanning, the sample was placed into a histology processing cassette and fixed by immersion in 10% neutral-buffered formalin (pH 7.2) for a minimum of 12 h for histopathologic processing. The sample was then embedded in paraffin, sectioned, mounted on a glass slide, and stained with hematoxylin and eosin (H&E) for histopathologic evaluation by light microscopy (Olympus BX–51, Optical Analysis Corporation, Nashua, NH, USA). Examples of histology images for each CP and T cell line are shown in Fig. 2.

From the optical histology images, nucleus and cell radii were estimated. For each CP and T, at least three histology images were selected to measure several nuclei areas using the ImageJ software. Assuming that the nuclei and cells have

circular shapes, their corresponding radii were computed from the area estimates. The mean nucleus and cell radii were estimated by measuring at least 150 of the largest nuclei and cells. From 2-D histology images, the nucleus and cell sizes are likely underestimated because the microtome's blade does not generally intersect the nucleus and/or cell centers, thus yielding circular structures with sizes smaller than the actual nuclei or cells. To limit this underestimation of the nucleus and cell radii, only the largest nuclei and cells were measured. Nucleus radii were evaluated for all four cell lines. Cell radii were evaluated for 4T1, JC, and LMTK CP. However, it was not possible to evaluate the cell radii for MAT CP and also for MAT, 4T1, JC, and LMTK T because the cytoplasm's contours were difficult to identify accurately.

The nucleus and cell volume fractions were approximated from the 2-D optical histology images. The number of nuclei N was calculated in the histology image area A_{im}. To obtain estimates of nucleus volume fractions (respectively, cell volume fractions), ϕ_N (ϕ_C), the volume occupied by nuclei (cells) was divided by the volume of the image using the estimated diameter of a cell d_C as the thickness dimension for the nucleus and cell volume fractions

$$\phi_N = \frac{NV_N}{A_{\text{im}} d_C}, \quad \phi_C = \frac{NV_C}{A_{\text{im}} d_C} \tag{1}$$

where V_N and V_C denote the nucleus and cell volumes assuming spherical shapes of nuclei and cells, respectively. This procedure was used for the nucleus volume fraction estimation of each cell line and the final values were an average from three histology images. As LMTK and MAT nucleus radii were similar in size, the LMTK cell radius was used for the MAT cell radius. As cell radii were missing for T, cell radii evaluated from CP were used as cell radii for T.

Ultrasonic scatterer parameters related to acoustic impedance from nuclei and cells were estimated from the H&E-stained histology images. H&E staining yields cytoplasm pink and nucleus blue with the intensity of pink or blue reflecting the protein or nucleic acid concentration, respectively [21]. A higher protein concentration in the medium appears pink and a higher nucleic acid concentration appears blue. The color intensity variation of this staining is interpreted as a difference in acoustic impedance. Pink and blue contrast values were estimated from cytoplasms and nuclei, respectively. The pink contrast (blue contrast corresponds to the intensity value in the first RGB channel (third RGB channel) from RGB histology images. This pink contrast (blue contrast) was estimated for cytoplasms and nuclei on five CP and five T histology images. The contrast was then averaged and normalized over the sum of the intensity values from the first, second, and third channels of the RGB image.

E. QUS Models

The ultrasonic parameters from two QUS models are compared: the spherical GM and the SFM. For the GM, the BSC is modeled using a spatial autocorrelation function describing the size, shape, acoustic properties, and distribution of the ultrasonic scatterers in the medium. The BSC was expressed as the product of the BSC in the Rayleigh limit and the backscatter form factor [22]. The form factor describes the frequency-dependent scattering in terms of the size, shape, and acoustic properties of the scatterers. The Gaussian form factor models a medium with continuous spatial changes in acoustic properties. The application of this model is valid for dilute media. The theoretical BSC using the GM formulation is given by [22]

$$\text{BSC}_{\text{GM}}(k) = \frac{k^4 V_s^2 \eta_Z}{4\pi^2} e^{-0.827 k^2 a_G^2} \tag{2}$$

where k is the wavenumber, η_Z is the acoustic concentration, and a_G is the effective scatterer radius with $V_s = 4\pi a_G^3/3$. The unknown parameters are the scatterer radius a_G and the acoustic concentration η_Z. Note that the fluid sphere model [22], which is closer to the SFM, provides similar results as the GM. However, in this study, the GM is preferred to the fluid sphere model because the GM has been more frequently used in other studies.

The SFM is based on the assumption that, at high scatterer volume fractions (i.e., dense media), interference effects are mainly caused by correlations between the spatial positions of individual scatterers (discrete scatterer with impedance differing from that of a homogeneous background medium). By considering an ensemble of identical spheres of radius a, the theoretical BSC for the SFM formulation is given by [4], [14]

$$\text{BSC}_{\text{SFM}}(k) = n \frac{k^4 V_s^2 \gamma_Z^2}{4\pi^2} \left[\frac{3}{(2ka)^3} j_1(2ka) \right]^2 S(k) \tag{3}$$

where V_s is the sphere volume and $n = \phi/V_s$ is the number density with ϕ the scatterer volume fraction, γ_Z the relative impedance contrast between scatterer and surrounding medium, and j_1 the spherical Bessel function of the first kind of order 1. S is the structure factor, which can be analytically obtained as described in [14, eqs. (A1)–(A4)] based on [23]. The unknown parameters are scatterer radius a, volume fraction ϕ, and relative impedance contrast γ_Z. The acoustic concentration for the SFM is calculated as: $\eta_Z = \phi \gamma_Z^2/(4\pi a^3/3)$.

The estimated values of the QUS-derived parameters were determined by fitting the theoretical BSCs to the measured BSC_{meas}, i.e., by minimizing the cost function

$$F = \frac{\sum_j \left\| \text{BSC}_{\text{meas}}(k_j) - \text{BSC}_{\text{theo}}(k_j) \right\|^2}{\sum_j \text{BSC}_{\text{meas}}(k_j)^2} \tag{4}$$

where BSC_{theo} is given by (2) for GM and by (3) for SFM. The cost functions are minimized over 25–55 MHz. The fitting procedure is performed using the minimization routine *fminsearch* without constraint in MATLAB (The MathWorks, Inc., Natick, MA, USA). The minimum cost function is evaluated using 20 initial random conditions ($a \in [1 - 10]$ μm, $\phi \in [0 - 0.7]$, $\gamma_Z \in [0.005 - 0.055]$, and $\eta_Z \in [1 - 10]$ dB.mm^{-3}).

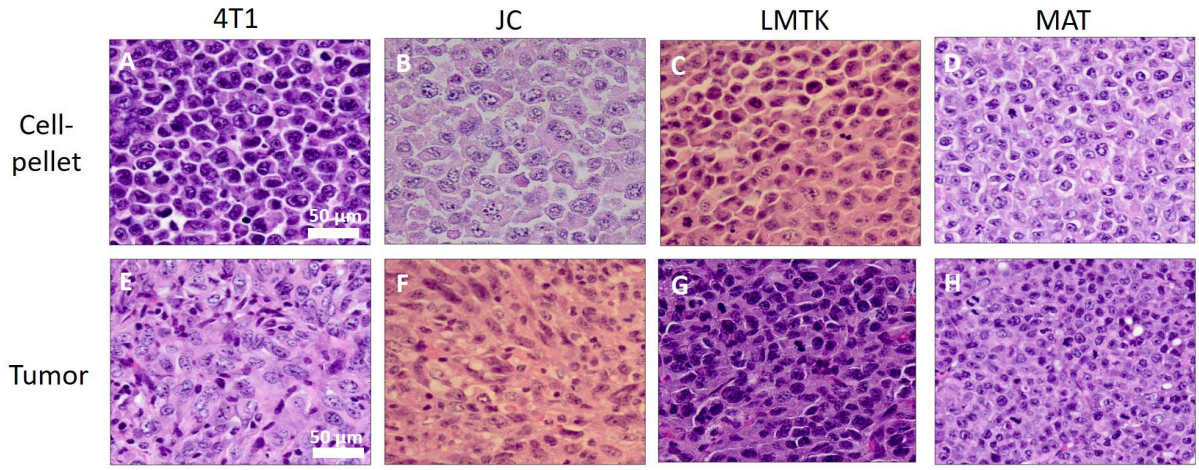

Fig. 2. Examples of *H* and *E*-stained histology images of 4T1, JC, LMTK, and MAT CP and T. Scale is the same for all images.

F. Optical Histology-Derived QUS Evaluations of CP Biophantoms and Ex Vivo T

As observed on the optical H&E-stained histology images (Fig. 2), the nuclei colors in the RGB images are quite variable, thus suggesting that the nuclei acoustic impedance may be quite variable from one nucleus to another. Therefore, it is possible that for some cells, the main ultrasonic scattering sites are the nuclei and for others, the cells themselves. In this study, three potential sources of ultrasonic scatterers are considered: nuclei only, cells only, and both nuclei and cells. Using the SFM (3), the calculated BSCs from nuclei only, cells only, and both nuclei and cells are generated from the optical histology-derived scatterer parameters. Then, the optical histology-derived scatterer parameters are compared against the QUS-derived scatterer parameters from experimental BSCs. In particular, we are interested in observing the scatterer outcome distributions (using the monodisperse SFM) in the presence of scattering from both cells and nuclei. The calculated BSCs from nuclei only BSC_N, cells only BSC_C, and both nuclei and cells BSC_{NC} are defined as

$$\mathrm{BSC}_N(k) = \mathrm{BSC}_{\mathrm{SFM}}(k, a_N, \phi_N) \tag{5}$$

$$\mathrm{BSC}_C(k) = \mathrm{BSC}_{\mathrm{SFM}}(k, a_C, \phi_C) \tag{6}$$

$$\mathrm{BSC}_{NC}(k) = w\mathrm{BSC}_N(k) + (1 - w)\mathrm{BSC}_C(k) \tag{7}$$

where the optical histology-derived parameters a_N, ϕ_N, a_C, and ϕ_C are the radii and volume fractions from nuclei and cells, respectively, and w is the nucleus/cell scattering ratio: $w = 0$ corresponds to scattering from cells only and $w = 1$ corresponds to scattering from nuclei only. A relative impedance contrast, γ_Z, of 0.03 for 4T1, JC, LMTK, and MAT CP was used. For tumors, γ_Z of 0.02 was used for 4T1 and JC T, 0.015 for LMTK T, and 0.035 for MAT T. These γ_Z values were chosen by comparing the calculated BSCs from nuclei and cells with the QUS-derived experimental BSCs for different γ_Z values (Fig. 3). An example of calculated BSCs for scattering from cells only, nuclei only, and both cells and nuclei (for indicated values of w) is shown in Fig. 4(A) using optical histology-derived nucleus and cell a and ϕ values of 4T1 CP.

Three strategies were used to calculate the optical histology-derived BSCs. These calculated BSCs were used to estimate the optically derived scatterer parameters, by inversion using SFM, for scattering from nuclei only, cells only, and both cells and nuclei. The comparison of the QUS-derived and optical histology-derived scatterer parameters will assist to determine whether the scattering is from nuclei only, cells only, or from both cells and nuclei for the cell type studied.

For strategy 1, 81 BSC_N (respectively, BSC_C) were generated using 81 uniform random a_N and ϕ_N (a_C and ϕ_C) values with a_N (a_C) ranging between [mean(a_N)±std(a_N)] ([mean(a_C)±std(a_C)]) and with ϕ_N (ϕ_C) ranging between [mean(ϕ_N)±0.25 mean(ϕ_N)] ([mean(ϕ_C)±0.10 mean(ϕ_C)]). An example of such an (a and ϕ) distribution for 4T1 CP is shown in Fig. 4(B) for w ratios of 0 (cells only), 0.1, 0.2, 0.3, 0.4, 0.5, 0.6, 0.7, 0.8, 0.9, and 1 (nuclei only); note that nucleus values congregate around (a_N and ϕ_N) and cell values around (a_C and ϕ_C). Eighty-one calculated BSC_{NC} were generated for each w ratio using the corresponding BSC_N and BSC_C. An example of BSCs obtained for 4T1 CP with strategy 1 is shown in Fig. 4(C). The same inversion process with the minimization of the cost function (4), as used experimentally, was realized to estimate the optical histology-derived parameters.

For strategy 2, the mean nucleus and cell radii and volume fractions from each CP and T cell line were used to calculate BSC_N, BSC_C, and BSC_{NC}. Uniform random noise was implemented to mimic BSC noise. The added noise had a mean of zero and a random variance increasing with frequency. The maximum variance increased from 1% to 5% of the maximum BSC from both cells and nuclei (with a w ratio of 0.5 of each structure). There were 81 realizations of noise for each cell line. A strategy 2 example of BSCs obtained for 4T1 CP is shown in Fig. 4(D). The same process, as used experimentally, was realized to estimate the optical histology-derived parameters.

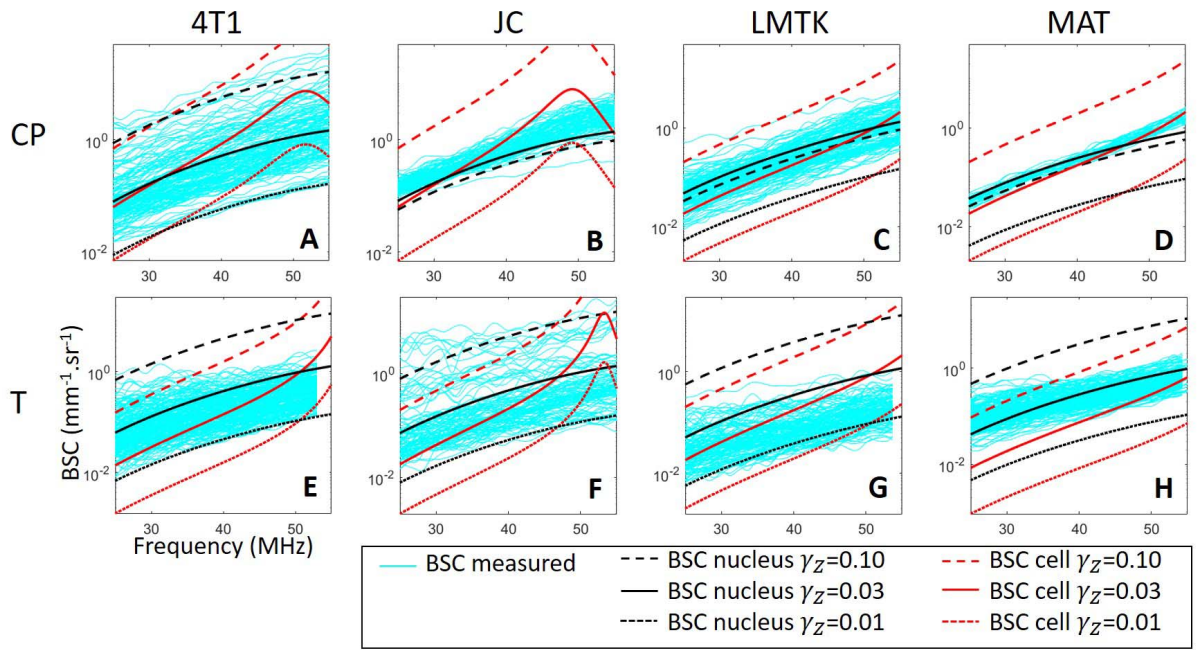

Fig. 3. QUS-derived mean BSCs (11 BSCs for each sample) for (A) and (E) 4T1, (B) and (F) JC, (C) and (G) LMTK, and (D) and (H) MAT (A)–(D) CP and (E)–(H) T (cyan lines). Superimposed on these plots are calculated BSCs from nuclei only (black continuous and dashed lines) and cells only (red continuous and dashed lines) using mean optical histology-derived a and ϕ estimates for each cell line and for three values of relative impedance contrast γ_Z (0.1, 0.03, and 0.01). CP denotes cell-pellet biophantom and T denotes tumor. Note that BSCs are plotted in log scale for sake of readability.

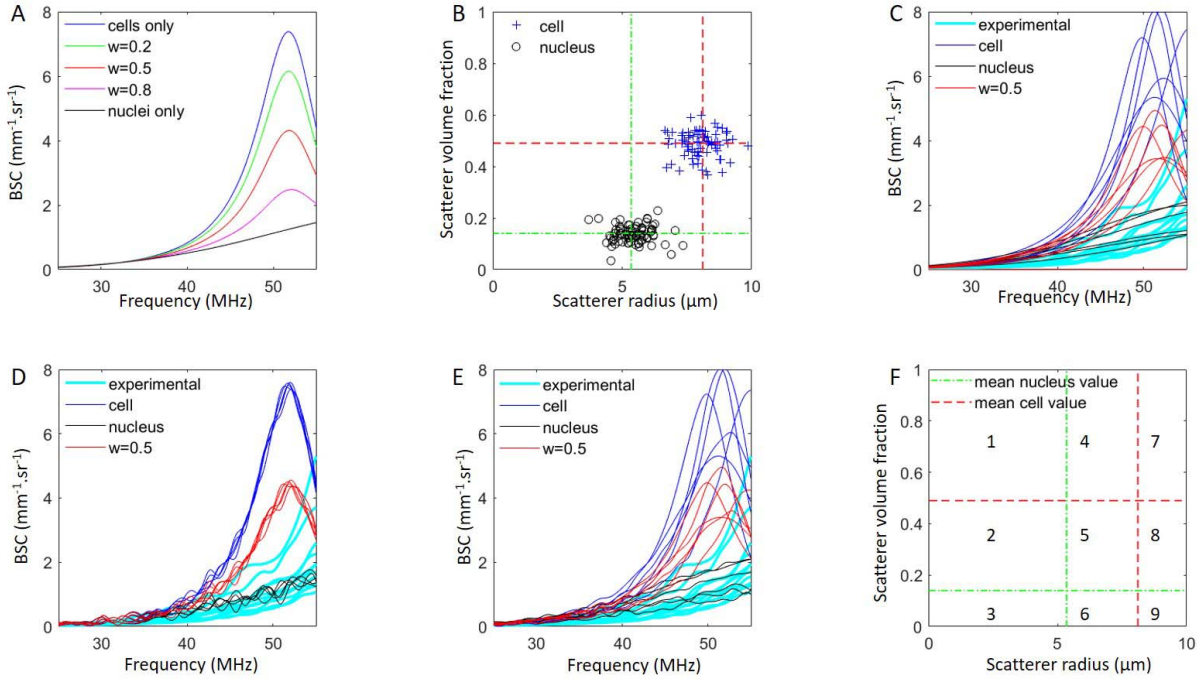

Fig. 4. (A) Calculated BSCs for various nucleus/cell scattering ratios w for 4T1 CP. (B) Using strategy 1, distribution of random nucleus and cell radii and volume fractions to theoretical BSCs for 4T1 CP. Superimposed examples of calculated BSCs and experimental BSCs for a 4T1 CP using (C) strategy 1, (D) strategy 2, and (E) strategy 3. (F) Numbered a versus ϕ grids for which green (a_N and ϕ_N) and red (a_C and ϕ_C) dashed lines correspond to the respective optical histology-derived mean values. CP denotes cell-pellet biophantom and T denotes tumor.

Strategy 3 combined the generation of 81 BSC_N (BSC_C) with 81 uniform random a_N and ϕ_N (a_C and ϕ_C) and random noise to mimic experimental BSCs. A strategy 3 example of BSCs obtained for 4T1 CP is shown in Fig. 4(E). The same process, as used experimentally, was realized to estimate the optical histology-derived parameters.

The objective behind the evaluation of calculated BSCs and the optical histology-derived parameters is to understand

TABLE III

OPTICAL HISTOLOGY-DERIVED NUCLEUS AND CELL RADII (a_N AND a_C, RESPECTIVELY) AND VOLUME FRACTIONS (ϕ_N AND ϕ_C, RESPECTIVELY), AS WELL AS NUCLEUS/CELL RADIUS RATIO a_N/a_C. a_N AND ϕ_N WERE EVALUATED FROM 4T1, JC, LMTK, AND MAT CP AND T. a_C AND ϕ_C WERE EVALUATED FROM 4T1, JC, AND LMTK CP. FOR THE RADII VALUES, THE MEAN AND STANDARD DEVIATION ARE PRESENTED. THE SYMBOL * IS USED WHEN THE a_C VALUE WAS NOT POSSIBLE TO EXTRACT AND THAT THE a_C VALUE FROM ANOTHER CELL TYPE OR FROM CP WAS USED INSTEAD. a_C FROM 4T1 CP WAS USED FOR 4T1 T, a_C FROM JC CP WAS USED FOR JC T, AND a_C FROM LMTK CP WAS USED FOR LMTK T, MAT CP, AND MAT T. CP DENOTES CELL-PELLET BIOPHANTOM AND T DENOTES TUMOR

Cell line	CP/T	a_N (μm)	ϕ_N	a_C (μm)	ϕ_C	a_N/a_C
4T1	CP	5.35 ± 0.56	0.14	8.12 ± 0.68	0.49	0.66
	T	4.96 ± 0.55	0.14	8.12*	0.64*	0.61*
JC	CP	5.49 ± 0.92	0.13	8.73 ± 1.85	0.52	0.63
	T	5.20 ± 0.71	0.14	8.73*	0.64*	0.60*
LMTK	CP	4.66 ± 0.46	0.15	7.25 ± 0.63	0.58	0.64
	T	4.62 ± 0.56	0.16	7.25*	0.64*	0.64*
MAT	CP	4.20 ± 0.41	0.13	7.25*	0.58*	0.60*
	T	4.37 ± 0.58	0.14	7.25*	0.65*	0.62*

the QUS-derived radius versus volume fraction distributions. In particular, the effect of scattering from both cells and nuclei evaluated with the monodisperse SFM is observed in these parameter distributions. The effect of noise on calculated BSCs is also considered in strategies 2 and 3.

III. RESULTS

A. Optical Histology-Derived Tissue Parameters of CP and T

The nucleus and cell radii and their volume fractions for each cell line were optically evaluated from histology images. These data are summarized in Table III. LMTK and MAT cell lines have a smaller nucleus and cell radii than 4T1 and JC CP along with higher cell volume fractions. These nucleus and cell radii differences are smaller for T, along with no nucleus volume fraction differences. Also, no a_N/a_C ratio differences among these cell lines are noted.

The pink and blue contrast values of nuclei and cells for CP and T cell lines are shown in Fig. 5. LMTK CP and JC T have pink contrast values of their nuclei and cells that are slightly higher than those of the other CP and T cell lines [Fig. 5(A) and (C)] along with lower blue contrast values [Fig. 5(B) and (D)]. LMTK T has higher nucleus and cell blue contrast values compared to the other cell lines [Fig. 5(B) and (D)].

B. QUS-Derived Tissue Parameters From BSC Evaluations of CP and T

1) Cell-Pellet Biophantoms: The mean radii, volume fractions, and acoustic concentrations estimated from CP's QUS-derived BSCs using two QUS models (GM and SFM) are summarized in Table IV. Using SFM, LMTK and MAT radii and volume fractions have lower relative errors compared to cell optical histology-derived values ($\leq$14% and $\leq$17%, respectively) than to nucleus optical histology-derived values. 4T1 and JC radii have low relative errors with nucleus radius ($\leq$10% and $\leq$7%, respectively) and cell volume fraction ($\leq$2% and $\leq$37%, respectively). Using GM, the four cell lines have small radii (close to 1 μm) and large acoustic concentrations compared to SFM. The standard deviations provided by SFM are quite large and observed on the (a and ϕ) scatterer parameter distributions [Figs. 6(A), 7(A), 8(A), and 9(A)] with large outcome spreads.

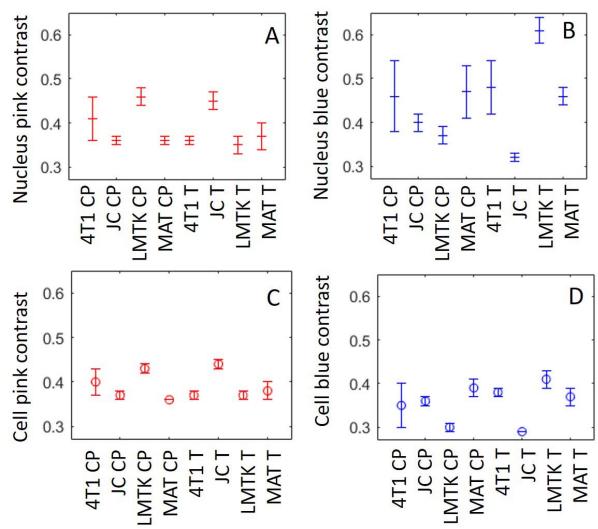

Fig. 5. Optical histology-derived pink and blue contrast estimates for the nucleus [(A) and (B), respectively] and cell cytoplasm [(C) and (D), respectively] for 4T1, JC, LMTK, and MAT CP and T. CP denotes cell-pellet biophantom and T denotes tumor.

2) Ex Vivo Tumors: The mean radii and volume fractions estimated from tumor's QUS-derived BSCs are summarized in Table V. All cell lines using the SFM have a small relative error for nucleus radii (<5%). However, even though the volume fractions are closer to nucleus volume fractions for 4T1, JC, MAT, and LMTK compared to cell volume fractions, the relative errors are quite high (>90% for 4T1, >33% for JC, >52% for LMTK, and >36% for MAT). QUS-derived parameters evaluated with GM have quite good agreement with nuclei for the four cell lines (relative error from 1.48 to 20.87%). For JC, LMTK, and MAT, SFM provides lower relative errors with nucleus radii than GM.

C. Comparison Between QUS-Derived a and ϕ From BSC Measurements and Optical Histology-Derived a and ϕ for CP and T Cell Lines

To describe (a and ϕ) distributions from experimental (QUS-derived from BSC measurements) and optical

TABLE IV

QUS-DERIVED SCATTERER RADII a, VOLUME FRACTIONS ϕ, AND ACOUSTIC CONCENTRATIONS η_Z ESTIMATED FROM EXPERIMENTAL BSCS OF 4T1, JC, LMTK, AND MAT CP USING SFM AND GM, THE TWO QUS MODELS. THE RELATIVE ERRORS COMPARE THE MEAN VALUES OF THE QUS-DERIVED PARAMETERS (a AND ϕ) WITH THEIR RESPECTIVE OPTICAL HISTOLOGY-DERIVED NUCLEUS (a_N AND ϕ_N) AND CELL (a_C AND ϕ_C) PARAMETERS. CP DENOTES CELL-PELLET BIOPHANTOM

CP cell line	QUS-derived parameters			Relative errors with nucleus (%)		Relative errors with cell (%)	
	a (μm)	ϕ	η_Z (dB/mm^3)	a_N	ϕ_N	a_C	ϕ_C
4T1 (SFM)	5.86 ± 2.14	0.48 ± 0.33	30.49 ± 14.22	9.46	255.11	25.33	1.46
4T1 (GM)	1.35 ± 1.24	-	52.56 ± 16.25	74.84	-	83.42	-
JC (SFM)	5.82 ± 1.54	0.33 ± 0.19	20.44 ± 12.57	6.01	152.92	33.33	36.77
JC (GM)	1.20 ± 0.86	-	53.95 ± 13.07	78.12	-	86.24	-
LMTK (SFM)	6.66 ± 1.68	0.50 ± 0.28	22.45 ± 14.84	42.92	234.53	8.14	13.48
LMTK (GM)	0.94 ± 0.73	-	56.68 ± 13.27	79.85	-	87.05	-
MAT (SFM)	6.81 ± 0.55	0.49 ± 0.13	15.77 ± 7.25	62.23	273.76	6.02	16.23
MAT GM	0.59 ± 0.05	-	66.32 ± 3.76	85.97	-	91.87	-

TABLE V

QUS-DERIVED SCATTERER RADII a, VOLUME FRACTIONS ϕ, AND ACOUSTIC CONCENTRATIONS η_Z ESTIMATED FROM EXPERIMENTAL BSCS OF 4T1, JC, LMTK, AND MAT T USING SFM AND GM, THE TWO QUS MODELS. THE RELATIVE ERRORS COMPARE THE MEAN VALUES OF THE QUS-DERIVED PARAMETERS (a AND ϕ) WITH THEIR RESPECTIVE OPTICAL HISTOLOGY-DERIVED NUCLEUS (a_N AND ϕ_N) AND CELL (a_C AND ϕ_C) PARAMETERS. T DENOTES TUMOR

T cell line	QUS-derived parameters			Relative errors with nucleus (%)		Relative errors with cell (%)	
	a (μm)	ϕ	η_Z (dB/mm^3)	a_N	ϕ_N	a_C	ϕ_C
4T1 (SFM)	4.82 ± 1.33	0.01 ± 0.09	11.82 ± 9.21	4.47	90.89	41.64	98.01
4T1 (GM)	5.03 ± 1.61	-	10.05 ± 8.42	1.48	-	38.01	-
JC (SFM)	4.94 ± 1.71	0.09 ± 0.18	15.06 ± 12.56	4.92	33.50	43.37	85.45
JC (GM)	4.11 ± 2.02	-	19.00 ± 15.00	20.87	-	52.87	-
LMTK (SFM)	4.40 ± 1.70	0.08 ± 0.22	13.59 ± 13.32	4.67	52.55	39.25	88.14
LMTK (GM)	4.19 ± 1.94	-	13.00 ± 12.28	9.26	-	42.18	-
MAT (SFM)	4.34 ± 1.54	0.09 ± 0.25	19.14 ± 12.93	0.60	36.54	40.09	86.94
MAT (GM)	3.98 ± 1.76	-	19.13 ± 14.28	8.91	-	45.10	-

histology-derived parameters, the numbered grids presented in Fig. 4(F) are used. For example, grid section 5 refers to outcomes with ϕ between ϕ_N and ϕ_C ($\phi_N < \phi_C$) and with a between a_N and a_C ($a_N < a_C$).

QUS-derived a and ϕ from experimental BSC measurements are directly compared with optical histology-derived a and ϕ on the a–ϕ nine-section grid [see Fig. 4(B) and (F)]. The a and ϕ axes are segmented by the mean a and ϕ cell and nucleus values derived from optical histology measurements and calculations. The notations on the a–ϕ grid are the a–ϕ coordinates that were derived experimentally from the QUS-derived BSC measurements and subsequent analysis strategies. For each CP and T cell line, the percentage of scatterers present in each of the nine sections was evaluated from QUS-derived and optical histology-derived a and ϕ values for cells only, nuclei only, and both cells and nuclei. These two nine-set percentages were pair-wise evaluated using the MATLAB function *corrcoef* to yield the Pearson correlation coefficient R and then the best correlation coefficient for each CP and T cell line.

1) QUS-Derived Scatterer Parameter Distributions: The (a and ϕ) distributions from 4T1, JC, LMTK, and MAT CP using SFM are presented in Figs. 6(A), 7(A), 8(A), and 9(A), respectively. The scatterer radii versus volume fractions experimental inversions from 4T1 CP [Fig. 6(A)] are mainly in sections 5 (30%), 3 (18%), and 1 + 4 + 7 (46%); from JC CP [Fig. 7(A)] are mainly in sections 5 (63%) and 1 + 4 (13%); from LMTK CP [Fig. 8(A)] are mainly in sections 5 + 8 (53%) and 4 + 7 (34%); and from MAT CP [Fig. 9(A)] are mainly in sections 5 (79%) and 7 (12%).

The scatterer radii versus volume fractions experimental inversions from 4T1 T [Fig. 6(F)] are mainly in sections 3 + 6 (98%); from JC T [Fig. 7(F)] are mainly in sections 3 + 6 (76%) and 5 (18%); from LMTK T [Fig. 8(F)] are mainly in sections 3 + 6 (84%) with a few in 1 + 4 + 7 (7%); and from MAT T [Fig. 9(F)] are mainly in sections 3 + 6 (86%) with a few in 1 + 4 + 7 (11%).

2) Strategy 1: Random a and ϕ Values: The optically derived scatterer parameters presented in this section were obtained using strategy 1: calculated BSCs from random values of a and ϕ. The calculated BSC distributions from cell structures provide a and ϕ values close to those cell parameters evaluated optically from histology [Figs. 6(B) and (G), 7(B) and (G), 8(B) and (G), and 9(B) and (G)]. The calculated BSC distributions from nucleus structures provide a and ϕ values close to those nucleus parameters evaluated optically from histology [Figs. 6(E) and (J), 7(E) and (J), 8(E) and (J), and 9(E) and (J)]. The calculated (a and ϕ) distributions from both nucleus and cell structures lead to outcomes, especially in sections 3, 5, and 1 + 4 + 7 [Figs. 6(C), (D), (H), and (I), 7(C), (D), (H), and (I), 8(C), (D), (H), and (I), and 9(C), (D), (H), and (I)].

The percentage of scatterers present in each grid section for scattering from cells only, nuclei only, and both cells and

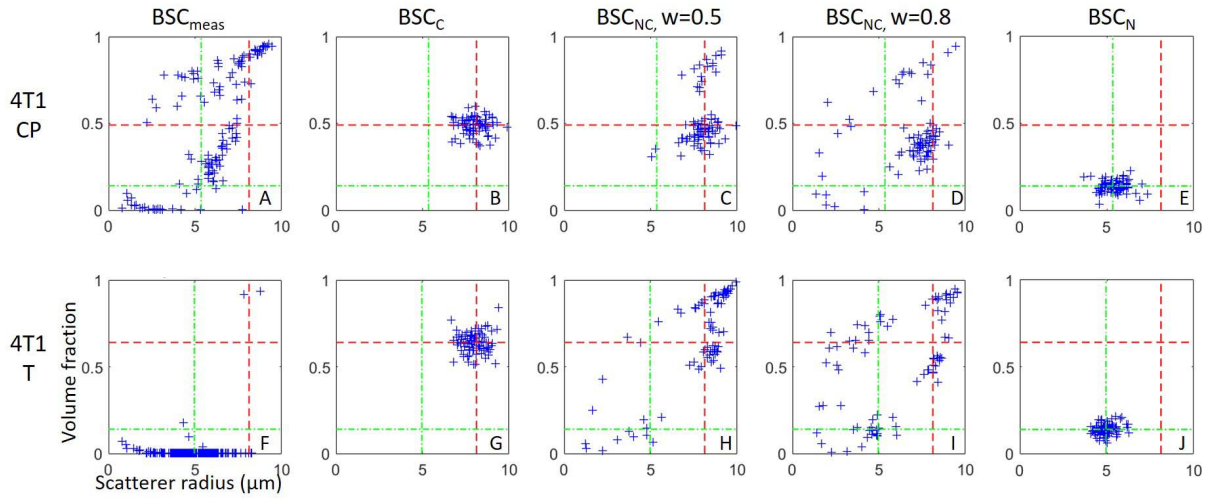

Fig. 6. 4T1 cell-pellet (top row) and 4T1 tumor (bottom row) scatterer radius versus volume fraction from QUS-derived BSCs [first column, (A) and (F)], calculated cell-only BSCs [BSC_C, second column, (B) and (G)], calculated cells and nuclei BSCs for $w = 0.5$ and 0.8 [BSC_{NC}, third and fourth column, (C), (D), (H), and (I)], and calculated nuclei-only BSCs [BSC_N, fifth column, (E) and (J)] obtained with strategy 1. The green (a_N and ϕ_N) and red (a_C and ϕ_C) dashed lines correspond to the mean optical histology-measured nucleus and cell radii and volume fractions, respectively.

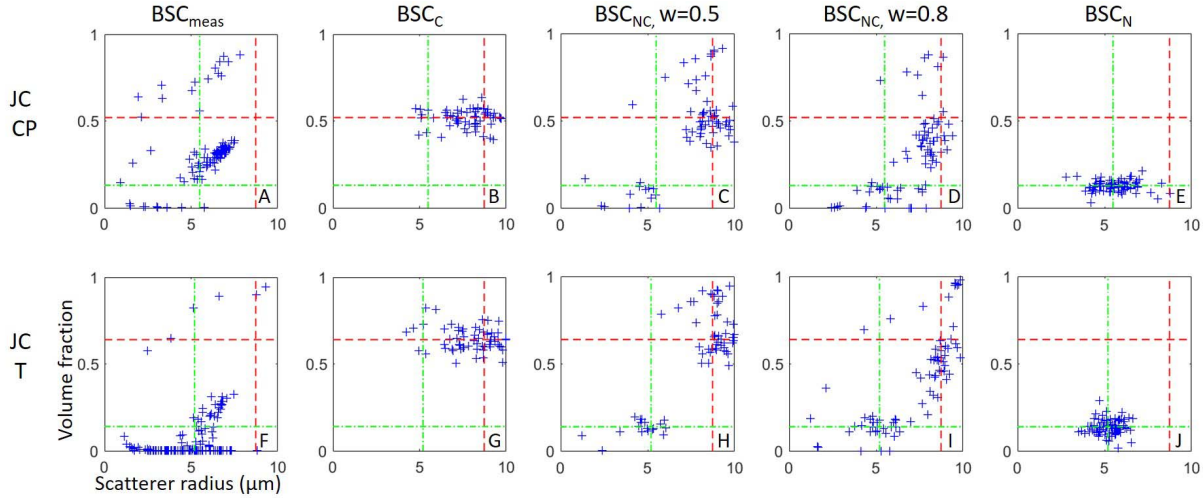

Fig. 7. JC cell-pellet (top row) and JC tumor (bottom row) scatterer radius versus volume fraction from QUS-derived BSCs [first column, (A) and (F)], calculated cell-only BSCs [BSC_C, second column, (B) and (G)], calculated cells and nuclei BSCs for $w = 0.5$ and 0.8 [BSC_{NC}, third and fourth column, (C), (D), (H) and (I)], and calculated nuclei-only BSCs [BSC_N, fifth column, (E) and (J)] obtained with strategy 1. The green (a_N and ϕ_N) and red (a_C and ϕ_C) dashed lines correspond to the mean optical histology-measured nucleus and cell radii and volume fractions, respectively. CP denotes cell-pellet biophantom and T denotes tumor.

nuclei was estimated, and their correlations with the experimental (a and ϕ) distributions are summarized in Table VI. For 4T1 and JC CP, these results highlight that the best correlations are for scattering from both cells and nuclei for which $w = 0.9$ ($R = 0.78$) for 4T1 and $w = 0.8$ ($R = 0.85$) for JC. LMTK and MAT CP present the best correlations for scattering from cells only ($R = 0.64$ for LMTK and $R = 0.59$ for MAT). 4T1, JC, and MAT T present the best correlations for scattering from nuclei only ($R = 0.46$ for 4T1, $R = 0.81$ for JC, and $R = 0.63$ for MAT). LMTK T presents the best correlations for scattering from both cells and nuclei with $w = 0.9$ ($R = 0.46$).

The optically derived scatterer parameter distributions using strategies 2 and 3 are in the Appendix (see supplementary materials).

IV. Discussion

The study's approach is to gain insight into the histologically identifiable cellular structure(s) involved in ultrasonic scattering by considering two scattering models (spherical GM and SFM) that yield quantitative measures of the nucleus and cell radii and their respective volume fractions (only for SFM). The general premise is that when ultrasonic scattering is assumed to be from nuclei only, the BSC is derived only from an incoherent contribution for which GM yields reasonable nucleus size estimates. When ultrasonic scattering is assumed to be from cells only, the BSC is derived from both incoherent and coherent contributions for which SFM yields reasonable cell size estimates. Also, when ultrasonic scattering is assumed to be from both cells and nuclei, a different approach is applied. Here, nucleus and cell radii

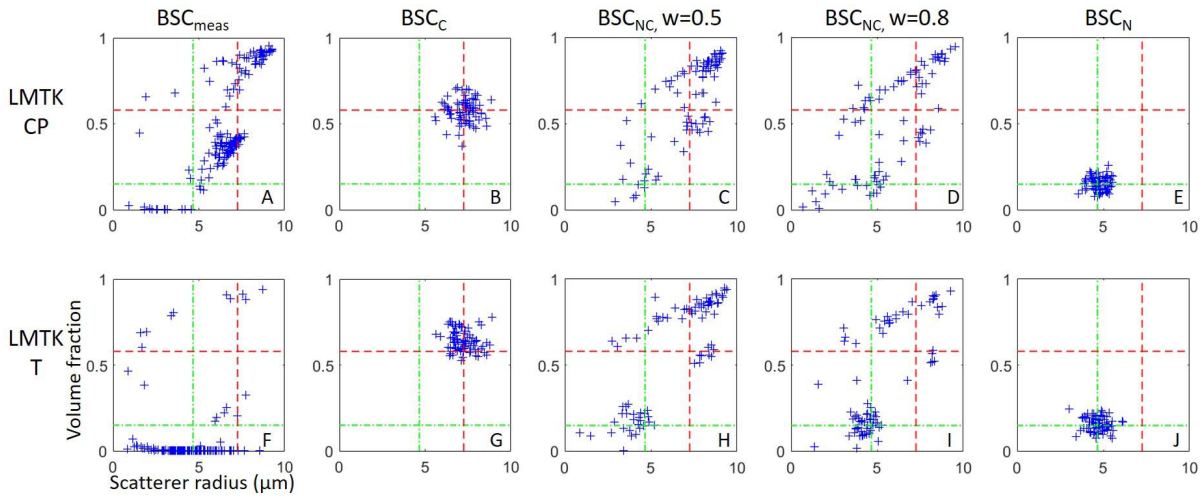

Fig. 8. LMTK cell-pellet (top row) and LMTK tumor (bottom row) scatterer radius versus volume fraction from QUS-derived BSCs [first column, (A) and (F)], calculated cell-only BSCs [BSC_C, second column, (B) and (G)], calculated cells and nuclei BSCs for $w = 0.5$ and 0.8 [BSC_{NC}, third and fourth column, (C), (D), (H) and (I)], and calculated nuclei-only BSCs [BSC_N, fifth column, (E) and (J)] obtained with strategy 1. The green (a_N and ϕ_N) and red (a_C and ϕ_C) dashed lines correspond to the mean optical histology-measured nucleus and cell radii and volume fractions, respectively. CP denotes cell-pellet biophantom and T denotes tumor.

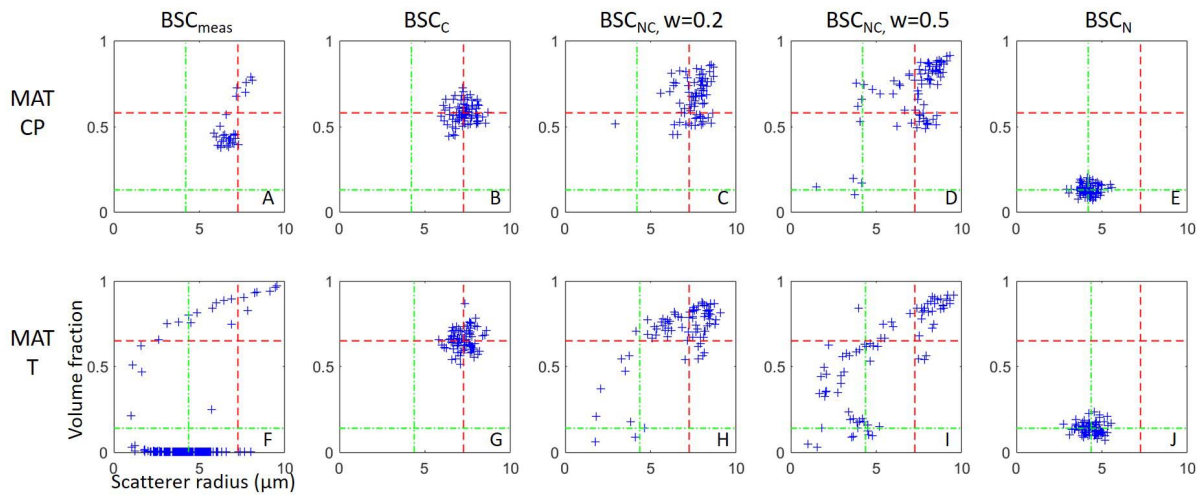

Fig. 9. MAT cell-pellet (top row) and MAT tumor (bottom row) scatterer radius versus volume fraction from QUS-derived BSCs [first column, (A) and (F)], calculated cell-only BSCs [BSC_C, second column, (B) and (G)], calculated cells and nuclei BSCs for $w = 0.2$ and 0.5 [BSC_{NC}, third and fourth column, (C), (D), (H) and (I)], and calculated nuclei-only BSCs [BSC_N, fifth column, (E) and (J)] obtained with strategy 1. The green (a_N and ϕ_N) and red (a_C and ϕ_C) dashed lines correspond to the mean optical histology-measured nucleus and cell radii and volume fractions, respectively. CP denotes cell-pellet biophantom and T denotes tumor.

(a_N and a_C) and their respective volume fractions (ϕ_N and ϕ_C) are derived optically from histology and used to calculate BSC for scattering from cells only, nuclei only, and from both cells and nuclei. Optically derived scatterer parameters were evaluated from these calculated BSC and compared to the experimental QUS-derived a_N, a_C, ϕ_N, and ϕ_C outcome parameters. This study evaluated four cell lines (4T1, JC, LMTK, and MAT) of both cell-pellet (CP) biophantoms and *ex vivo* tumors (T).

The first observation is that the QUS-derived (a and ϕ) distributions obtained for all cell lines and especially for CP are quite spread [Figs. 6(A), 7(A), 8(A), and 9(A)]. Also, some of the tumor outcomes yield volume fractions close to zero, which does not correspond to a physical scattering site [Figs. 6(F), 7(F), 8(F), and 9(F)]. There are several considerations to explain volume fractions located near zero or a large distribution of the outcomes: 1) these outcome data may correspond to local minima, even if the minimal cost function were evaluated on 20 initial conditions, and 2) there is neither a unique scattering structure (i.e., cell and nucleus) nor a monodisperse one that is not considered with the SFM.

A. Cellular Structure(s) Involved in Ultrasonic Scattering

Best correlations (Table VI) have assisted to identify which optical histology-derived (a and ϕ) distributions are closest to the QUS-derived (a and ϕ) distributions for cells only, nuclei only, and both cells and nuclei.

TABLE VI
BEST CORRELATION COEFFICIENTS (PEARSON R) BETWEEN THE PERCENTAGE OF NUMERICAL SCATTERERS PRESENT IN EACH GRID SECTION [FIG. 4(F)] FOR SCATTERING FROM CELLS ONLY, NUCLEI ONLY, AND BOTH CELLS AND NUCLEI WITH THE EXPERIMENTAL (a AND ϕ) DISTRIBUTION FOR EACH CP AND T CELL LINES (CP/T). CP DENOTES CELL-PELLET BIOPHANTOM, T DENOTES TUMOR, N DENOTES NUCLEI ONLY, C DENOTES CELLS ONLY, AND NC DENOTES BOTH NUCLEI AND CELLS

	Strategy 1		Strategy 2		Strategy 3	
	best R	corresponding w	best R	corresponding w	best R	corresponding w
4T1 CP	0.77	0.9, NC	0.68	0.1, NC	0.74	0.8, NC
4T1 T	0.46	1, N	0.31	1, N	0.41	1, N
JC CP	0.85	0.8, NC	0.97	0.4, NC	0.93	1, N
JC T	0.81	1, N	0.58	1, N	0.49	1, N
LMTK CP	0.64	0, C	0.88	0, C	0.80	0.1, NC
LMTK T	0.46	0.9, NC	0.20	1, N	0.25	1, N
MAT CP	0.59	0, C	0.69	0, C	0.69	1, N
MAT T	0.63	1, N	0.19	1, N	0.11	1, N

Pearson's correlation coefficients between the optical histology- and QUS-derived (a and ϕ) distributions from *ex vivo* tumors of the four cell lines and the three analysis strategies (Table VI and Figs. 6–9) suggest that tumor scattering is mainly from nuclei, except for LMTK T for strategy 1 which provided a best correlation for scattering from both nuclei and cells.

The *ex vivo* tumors are thus considered dilute media because the scatterer parameter radius and acoustic concentration outcomes for both GM and SFM are similar [6], suggesting the dominance of incoherent backscattering. This observation is corroborated with the GM-evaluated scatterer radii being similar to the optical histology-derived nucleus radii (relative error between 1.48% and 20.87%, Table V). The SFM-evaluated scatterer radii are also close to the optical histology-derived nucleus radii (relative error between 0.60% and 4.92%, Table V). However, the nucleus volume fractions are quite different (relative error between 33.50% and 90.89%, Table V). It should be noted that for dilute media, the structure function (S) is close to unity, which leads to challenges extracting correctly the scatterer volume fraction and relative impedance contrast from the acoustic concentration.

Pearson's correlation coefficients between optical histology- and QUS-derived (a and ϕ) distributions from LMTK and MAT CP with strategies 1 and 2 (Table VI and Figs. 8 and 9) suggest scattering from cells only. However, for strategy 3, the best correlation for LMTK CP is for scattering from both nuclei and cells and the best correlation for MAT CP is for scattering from nuclei only. Similarly, the best correlations between optical histology- and QUS-derived (a and ϕ) distributions from 4T1 and JC CP with strategies 1 and 2 (Table VI and Figs. 6 and 7) suggest scattering from both cells and nuclei. Strategy 3 provides the best correlation for 4T1 CP for scattering from both nuclei and cells, but the best correlation for JC CP is for scattering from nuclei only. Based on these observations, strategy 3 (includes variations from a and ϕ values as well as from adding noise) may not be appropriate for comparison of experimental results.

The CP biophantoms are considered dense media because the GM-evaluated scatterer radii are underestimated and the acoustic concentrations are overestimated [6], suggesting that both incoherent and coherent backscatter components are present. Moreover, the GM-evaluated scatterer radius is close to 1 μm (Table IV), thus not corresponding neither to nucleus nor to cell radii. The optical histology-derived nucleus volume fractions are similar between CP and T, suggesting for the CP case that either cell structure or both nucleus and cell structures are involved in ultrasonic scattering. The mean MAT and LMTK CP scatterer optical histology-derived parameters are similar to whole cell parameters (relative error $\leq$17%, Table IV). The mean 4T1 and JC CP scatterer radius parameters are similar to the optical histology-derived nucleus radii (relative error $<$ 10%), but the volume fraction estimates are quite different from optical histology-derived nucleus volume fractions (relative error $>$152%) and closer to the cell volume fractions (relative error $<$37%, Table IV).

As a concluding comment, the (a and ϕ) distribution results with strategies 1 and 2 are (almost) in agreement with the mean scatterer parameters (Tables IV–VI). These results suggest that nuclei only is the main structure involved in ultrasonic scattering from 4T1, JC, LMTK, and MAT T that cells only are the main structure involved in ultrasonic scattering from LMTK and MAT CP and that both cells and nuclei are involved in ultrasonic scattering from 4T1 and JC CP.

B. Differences Between CP and T That May Explain a Difference in the Structure Involved in Ultrasonic Scattering

The scattering structures are different between CP and T, CP providing insight into dense media and T providing insight into dilute media. Moreover, if the nucleus appears to be a major scattering source from 4T1 and JC CP and T, then for LMTK and MAT, a difference in the scatterer source is observed with cells for CP and nuclei for T.

The nucleus radii from T show a slight increase for LMTK and MAT compared to CP along with a slight decrease of 4T1 and JC CP, reducing the radii differences among 4T1/JC and LMTK/MAT (Table III). There are no contrast differences between 4T1/JC and LMTK/MAT, which may explain a change of scattering structure for LMTK and MAT (Fig. 5). However, the main difference between CP and T may be the cell relative impedance contrast, γ_Z. Indeed, from histology images of CP, spaces are observed between cells [Fig. 2(A)–(D)]. These spaces are certainly filled with DPBS/saline during ultrasonic acquisitions. For T

[Fig. 2(E)–(H)], there are no spaces between cells, so the surrounding medium of cells is certainly occupied by other cytoplasm and eventually extracellular matrix, possibly leading to a lower relative impedance contrast between cells, and certainly much lower than the relative impedance contrast between cytoplasm and DPBS/saline from CP. This may explain why the scattering structure from MAT and LMTK T is not the cell (or both cell and nucleus) and why there may be no contribution of the cell for 4T1 and JC T.

This difference in the structure involved in ultrasonic scattering from CP and T of the same cell line suggests that the CP (at least for the four cell lines evaluated herein) may not be good tumor models. The use of spheroids of cells with extracellular matrix presence and cell interactions may provide a better tumor model.

C. Limits of the Study

Two ultrasonic scattering models (GM and SFM) were used to elucidate the scattering mechanism(s). Both models assumed monodisperse scatterers. Polydisperse models, and perhaps a wider range of models, should be included in future studies to further assist with mechanistic understanding of ultrasonic scattering. Optical histology-derived parameter outcomes were compared to QUS-derived parameter outcomes from experimental BSCs. To generate these calculated BSC, a combination of BSC from nuclei and cells was used (7). The nucleus and cell radii and volume fractions were optically estimated. However, the relative impedance contrast was chosen to be identical for cells and nuclei, which poses a serious limitation particularly as it can also affect the nucleus/cell scattering ratio w term. A future improvement could be the addition of a direct impedance contrast assessment using acoustic microscopy, for example, [24], [25].

Correlation analyses between QUS-derived (a and ϕ) parameter outcomes and optical histology-derived (a and ϕ) parameter outcomes were performed utilizing the a versus ϕ nine-section grid [Fig. 4(F)]. On this grid, the a and ϕ axes were segmented by the mean a and ϕ cell and nucleus values. However, with this definition, an outcome close to cell radii and volume fractions may be in section 4, 5, 7, or 8 and an outcome close to nucleus radii and volume fractions may be in section 2, 3, 5, or 8. The correlation of the percentage of outcomes in each grid section could then introduce a bias if there were a shift of the outcome positions. Other analysis approaches might provide more robust a–ϕ distributions.

To obtain insight about the cellular structure(s) involved in ultrasonic scattering, this study was conducted using simple models containing mostly cells: cell-pellet biophantoms containing cells only and the *ex vivo* tumors containing cells and also extracellular matrix. For *in vivo* tumors, the presence of blood vessels, connective tissue, and lymphatic structures would affect the scattering, likely resulting in more complex scattering. Such additional intercellular materials would likely lead to QUS-derived parameter outcomes more difficult to interpret and compare with optical histology-measured data, even with a monodisperse model.

V. Conclusion

The study's objective was to gain insight into specific cellular structure(s) involved in ultrasonic scattering. Indeed, there is a significant scientific value to elucidate the ultrasonic scattering structure(s), particularly at the cellular scale to determine, for example, whether CP biophantoms are equivalent models of *ex vivo* tumors for tissue characterization applications. Ultrasonic scatterer parameters from four cell lines of cell-pellet biophantoms and *ex vivo* tumors were evaluated using two scattering models (SFM and GM) and compared to the optical histology-measured parameters (cells and nuclei radii and volume fractions) to evaluate whether the structure(s) involved in ultrasonic scattering is(are) cells only or nuclei only. To determine whether both cells and nuclei were involved in ultrasonic scattering, BSCs were calculated using a simple model with the optical histology-measured parameters as inputs. The optical histology scatterer parameter distributions derived from these calculated BSCs were compared to the QUS-derived scatterer parameters. The results highlight that nuclei appear to be the main structure involved in ultrasonic scattering for 4T1, JC, LMTK, and MAT tumors; cells appear to be the structure involved in ultrasonic scattering for LMTK and MAT cell pellets; and cells and nuclei appear to be the structures involved in ultrasonic scattering for 4T1 and JC cell pellets. In future studies, the cellular structure(s) involved in ultrasonic scattering may be evaluated for more cell lines to further elucidate scattering structure(s) from one cell line to another. The evaluation of the cellular structure(s) involved in ultrasonic scattering should also involve *in vivo* tumors.

Acknowledgment

The authors would like to thank R. Miller, DVM, J. Kelly, Jake Berndt, and Prof. A. Han for the help with cell culture, animal care, and ultrasonic acquisitions.

References

[1] A. Han, R. Abuhabsah, J. P. Blue, Jr., S. Sarwate, and W. D. O'Brien, Jr., "Ultrasonic backscatter coefficient quantitative estimates from high-concentration Chinese hamster ovary cell pellet biophantoms," *J. Acoust. Soc. Amer.*, vol. 130, no. 6, pp. 4139–4147, 2011, doi: 10.1121/1.3655879.

[2] A. Han, R. Abuhabsah, R. J. Miller, S. Sarwate, and W. D. O'Brien, "The measurement of ultrasound backscattering from cell pellet biophantoms and tumors *ex vivo*," *J. Acoust. Soc. Amer.*, vol. 134, no. 1, pp. 686–693, Jul. 2013, doi: 10.1121/1.4807576.

[3] A. Han and W. D. O'Brien, Jr., "Structure function for high-concentration biophantoms of polydisperse scatterer sizes," *IEEE Trans. Ultrason., Ferroelectr., Freq. Control*, vol. 62, no. 2, pp. 303–318, Feb. 2015.

[4] E. Franceschini and R. Guillermin, "Experimental assessment of four ultrasound scattering models for characterizing concentrated tissue-mimicking phantoms," *J. Acoust. Soc. Amer.*, vol. 132, no. 6, pp. 3735–3747, 2012, doi: 10.1121/1.4765072.

[5] E. Franceschini, R. Guillermin, F. Tourniaire, S. Roffino, E. Lamy, and J.-F. Landrier, "Structure factor model for understanding the measured backscatter coefficients from concentrated cell pellet biophantoms," *J. Acoust. Soc. Amer.*, vol. 135, no. 6, pp. 3620–3631, 2014, doi: 10.1121/1.4876375.

[6] E. Franceschini, R. de Monchy, and J. Mamou, "Quantitative characterization of tissue microstructure in concentrated cell pellet biophantoms based on the structure factor model," *IEEE Trans. Ultrason., Ferroelectr., Freq. Control*, vol. 63, no. 9, pp. 1321–1334, Sep. 2016.

[7] A. Cristea, E. Franceschini, F. Lin, J. Mamou, C. Cachard, and O. Basset, "Quantitative characterization of concentrated cell pellet biophantoms using statistical models for the ultrasound echo envelope," *Phys. Proc.*, vol. 70, pp. 1091–1095, Jan. 2015. [Online]. Available: http://www.sciencedirect.com/science/article/pii/S1875389215009748

[8] G. J. Czarnota and M. C. Kolios, "Ultrasound detection of cell death," *Imag. Med.*, vol. 2, no. 1, pp. 17–28, Feb. 2010. [Online]. Available: https://www.openaccessjournals.com/abstract/ultrasound-detection-of-cel%l-death-10977.html

[9] R. M. Vlad, R. K. Saha, N. M. Alajez, S. Ranieri, G. J. Czarnota, and M. C. Kolios, "An increase in cellular size variance contributes to the increase in ultrasound backscatter during cell death," *Ultrasound Med. Biol.*, vol. 36, no. 9, pp. 1546–1558, 2010. [Online]. Available: http://www.sciencedirect.com/science/article/pii/S0301562910002553

[10] M. C. Kolios, G. J. Czarnota, M. Lee, J. W. Hunt, and M. D. Sherar, "Ultrasonic spectral parameter characterization of apoptosis," *Ultrasound Med. Biol.*, vol. 28, no. 5, pp. 589–597, May 2002. [Online]. Available: http://www.sciencedirect.com/science/article/pii/S0301562902004921

[11] R. M. Vlad, N. M. Alajez, A. Giles, M. C. Kolios, and G. J. Czarnota, "Quantitative ultrasound characterization of cancer radiotherapy effects *in vitro*," *Int. J. Radiat. Oncol.*Biol.*Phys.*, vol. 72, no. 4, pp. 1236–1243, Nov. 2008. [Online]. Available: http://www.sciencedirect.com/science/article/pii/S0360301608031131

[12] P. Muleki-Seya *et al.*, "High-frequency quantitative ultrasound spectroscopy of excised canine livers and mouse tumors using the structure factor model," *IEEE Trans. Ultrason., Ferroelectr., Freq. Control*, vol. 63, no. 9, pp. 1335–1350, Sep. 2016.

[13] D. Savéry and G. Cloutier, "A point process approach to assess the frequency dependence of ultrasound backscattering by aggregating red blood cells," *J. Acoust. Soc. Amer.*, vol. 110, no. 6, pp. 3252–3262, 2001, doi: 10.1121/1.1419092.

[14] V. Twersky, "Low-frequency scattering by correlated distributions of randomly oriented particles," *J. Acoust. Soc. Amer.*, vol. 81, no. 5, pp. 1609–1618, 1987, doi: 10.1121/1.394513.

[15] A. D. Pawlicki, A. J. Dapore, S. Sarwate, and W. D. O'Brien, "Three-dimensional impedance map analysis of rabbit liver," *J. Acoust. Soc. Amer.*, vol. 130, no. 5, Nov. 2011, Art. no. EL334, doi: 10.1121/1.3646024.

[16] L. R. Taggart, R. E. Baddour, A. Giles, G. J. Czarnota, and M. C. Kolios, "Ultrasonic characterization of whole cells and isolated nuclei," *Ultrasound Med. Biol.*, vol. 33, no. 3, pp. 389–401, 2007. [Online]. Available: https://www.sciencedirect.com/science/article/pii/S0301562906017790

[17] J. W. Hunt, A. E. Worthington, and A. T. Kerr, "The subtleties of ultrasound images of an ensemble of cells: Simulation from regular and more random distributions of scatterers," *Ultrasound Med. Biol.*, vol. 21, no. 3, pp. 329–341, Jan. 1995. [Online]. Available: http://www.sciencedirect.com/science/article/pii/0301562994001203

[18] G. J. Czarnota *et al.*, "Ultrasonic biomicroscopy of viable, dead and apoptotic cells," *Ultrasound Med. Biol.*, vol. 23, no. 6, pp. 961–965, Jan. 1997. [Online]. Available: http://www.sciencedirect.com/science/article/pii/S0301562997000677

[19] G. J. Czarnota *et al.*, "Ultrasound imaging of apoptosis: High-resolution non-invasive monitoring of programmed cell death *in vitro*, *in situ* and *in vivo*," *Brit. J. Cancer*, vol. 81, no. 3, pp. 520–527, Oct. 1999. [Online]. Available: https://www.nature.com/articles/6690724

[20] K. A. Wear *et al.*, "Interlaboratory comparison of ultrasonic backscatter coefficient measurements from 2 to 9 MHz," *J. Ultrasound Med.*, vol. 24, no. 9, pp. 1235–1250, 2005, doi: 10.7863/jum.2005.24.9.1235.

[21] J. Mamou, M. L. Oelze, W. D. O'Brien, and J. F. Zachary, "Identifying ultrasonic scattering sites from three-dimensional impedance maps," *J. Acoust. Soc. Amer.*, vol. 117, no. 1, pp. 413–423, 2005, doi: 10.1121/1.1810191.

[22] M. F. Insana, D. G. Brown, "Acoustic scattering theory applied to soft biological tissues," in *Ultrasonic Scattering in Biological Tissues*. Boca Raton, FL, USA: CRC Press, 1993, pp. 75–124.

[23] M. S. Wertheim, "Exact solution of the Percus–Yevick integral equation for hard spheres," *Phys. Rev. Lett.*, vol. 10, no. 8, pp. 321–323, Apr. 1963, doi: 10.1103/PhysRevLett.10.321.

[24] N. Hozumi, S. Yoshida, and K. Kobayashi, "Three-dimensional acoustic impedance mapping of cultured biological cells," *Ultrasonics*, vol. 99, Nov. 2019, Art. no. 105966. [Online]. Available: https://www.sciencedirect.com/science/article/pii/S0041624X18306486

[25] E. B. Prastika *et al.*, "Three-dimensional acoustic impedance mapping of human skin by improved time–frequency domain analysis," *Jpn. J. Appl. Phys.*, vol. 60, May 2021, Art. no. SDDE22, doi: 10.35848/1347-4065/abf512.

Pauline Muleki-Seya received the M.S. degree in acoustics from the University of Le Mans, Le Mans, France, in 2011 and the Ph.D. degree in acoustics from the University of Lyon, Villeurbanne, France, in 2014.

From 2015 to 2016, 2016 to 2017, and 2017 to 2019, she was a Postdoctoral Fellow at the Laboratory of Mechanics and Acoustics, Marseille, France, the Bioacoustics Research Laboratory, Department of Electrical and Computer Engineering, University of Illinois at Urbana–Champaign, and Physics for Medicine Paris, respectively, conducting research on quantitative ultrasound techniques on soft tissues and microbubble detection for ultrasound localization microscopy. Since 2019, she has been a Researcher with the CREATIS Laboratory, French National Center for Scientific Research, University of Lyon. Her research interests include quantitative ultrasound techniques, ultrasound tissue, and microvasculature characterization.

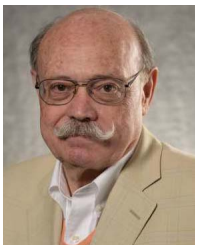

William D. O'Brien, Jr. (Life Fellow, IEEE) received the B.S., M.S., and Ph.D. degrees from the University of Illinois at Urbana–Champaign, Urbana, IL, USA, in 1966, 1968, and 1970, respectively.

From 1971 to 1975, he worked with the Bureau of Radiological Health (currently Center for Devices and Radiological Health) of the U.S. Food and Drug Administration. In 1975, he joined the University of Illinois Faculty. Since 2012, he has been with the Donald Biggar Willet Professor Emeritus of Engineering and a Research Professor of Electrical and Computer Engineering, Bioengineering, and the Carle Ilinois College of Medicine. His research interests involve many areas of ultrasound–tissue interaction, including biological effects and quantitative ultrasound imaging for which he has published 439 articles.

Dr. O'Brien is a fellow of the Acoustical Society of America and the American Institute of Ultrasound in Medicine and a Founding Fellow of the American Institute of Medical and Biological Engineering. He was a recipient of the ASA Silver Medal in Biomedical Acoustics in 2021, the IEEE Centennial Medal in 1984, the AIUM Presidential Recognition Awards in 1985 and 1992, the AIUM/WFUMB Pioneer Award in 1988, the IEEE Outstanding Student Branch Counselor Award for Region 4 in 1989, the AIUM Joseph H. Holmes Basic Science Pioneer Award in 1993, the IEEE Ultrasonics, Ferroelectrics, and Frequency Control Society Distinguished Lecturer from 1997 to 1998, the IEEE Ultrasonics, Ferroelectrics, and Frequency Control Society's Achievement Award in 1998, the IEEE Millennium Medal in 2000, the IEEE Ultrasonics, Ferroelectrics, and Frequency Control Society's Distinguished Service Award in 2003, the AIUM William J. Fry Memorial Lecture Award in 2007, the IEEE Ultrasonics, Ferroelectrics, and Frequency Control Society's Rayleigh Award in 2008, and the UIUC ECE Department's Distinguished Alumni Award in 2020. He has served as the President for the IEEE Sonics and Ultrasonics Group (currently the IEEE UFFC Society) from 1982 to 1983, the Editor-in-Chief for the IEEE TRANSACTIONS ON ULTRASONICS, FERROELECTRICS, AND FREQUENCY CONTROL from 1984 to 2001, and the President for the American Institute of Ultrasound in Medicine from 1988 to 1991.